Photonic Gene Circuits by Optically Addressable siRNA-Au Nanoantennas

Somin Eunice Lee,[†,§] Darryl Y. Sasaki,[‡] Younggeun Park,[†] Ren Xu,[§,⊥] James S. Brennan,[‡] Mina J. Bissell,[§] and Luke P. Lee[†,*]

[†]UCSF/UCB Joint Graduate Group in Bioengineering, Berkeley Sensor & Actuator Center, Department of Bioengineering, University of California—Berkeley, Berkeley, California, United States, [‡]Material Science Division, Sandia National Laboratories, Livermore, California, United States, [§]Life Sciences Division, Lawrence Berkeley National Laboratories, Berkeley, California, United States, and [⊥]Department of Molecular and Biomedical Pharmacology, University of Kentucky, Lexington, Kentucky, United States

ABSTRACT The precise perturbation of gene circuits and the direct observation of signaling pathways in living cells are essential for both fundamental biology and translational medicine. Current optogenetic technology offers a new paradigm of optical control for cells; however, this technology relies on permanent genomic modifications with light-responsive genes, thus limiting dynamic reconfiguration of gene circuits. Here, we report precise control of perturbation and reconfiguration of gene circuits in living cells by optically addressable siRNA-Au nanoantennas. The siRNA-Au nanoantennas fulfill dual functions as selectively addressable optical receivers and biomolecular emitters of small interfering RNA (siRNA). Using siRNA-Au nanoantennas as optical inputs to existing circuit connections, photonic gene circuits are constructed in living cells. We show that photonic gene circuits are modular, enabling subcircuits to be combined on-demand. Photonic gene circuits open new avenues for engineering functional gene circuits useful for fundamental bioscience, bioengineering, and medical applications.

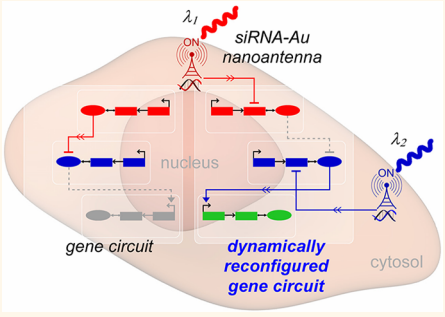

KEYWORDS: siRNA · RNA interference · optogenetics · plasmonics · gene delivery · gene therapy · gold nanorod

Gene circuits, consisting of interconnected genes and proteins, give rise to cell functions essential in signaling, growth, differentiation, and apoptosis. Despite some initial success, many important gene circuits remain incompletely understood. Increased understanding of information processing and operation of gene circuits should advance therapeutic strategies for reconfiguring gene circuits involved in disease progression and cancer. A major challenge is probing native gene circuits with high signal fidelity. Top-down probing approaches utilize an external input signal and essentially treat a living cell as an input—output "black box". Ideally, the output signal should be directly correlated to the input signal. However, signal distortions—time delays, noise, and signal magnitude reductions—can confound this input—output relationship,[1] hindering temporally precise modulation of gene circuits and limiting dynamic reconfiguration of gene circuits in living cells.

Intracellular approaches that enable temporally precise modulation of native gene circuits and dynamic reconfiguration of existing circuit connections will have widespread applications in fundamental biology and translational medicine. Optical input signals are a promising interface to gene circuit connections. Current optogenetic methods to interface with living cells have so far relied on genomic modifications (*i.e.*, mutations, overexpression) to permanently encode these cells with light-responsive genes,[2] limiting on-demand reconfiguration of gene circuits in living cells. To enable on-demand circuit reconfiguration, remotely controlled inputs to gene circuits are required. Previously, remote control of biomolecules has been demonstrated by inductive coupling of radio frequencies to nanocrystal antennas.[3] Recently, remote optical control of biomolecules, such as DNA[4] and siRNA,[5] has been demonstrated by coupling optical frequencies to resonant optical nanoantennas.[4−16] By receiving and focusing freely propagating optical radiation into localized energy, resonant optical nanoantennas efficiently convert absorbed optical energy into surface-localized heat, otherwise known as photothermal effect.[17−22] When biomolecules are functionalized to the surface of the nanoantenna, this optically generated, surface-localized heat can be used to liberate (*i.e.*, emit) biomolecules from the nanoantenna. Inside of living cells, optical silencing of genes (Figure S9) has been previously

* Address correspondence to lplee@berkeley.edu.

Received for review April 20, 2012 and accepted July 24, 2012.

Published online July 24, 2012
10.1021/nn301744x

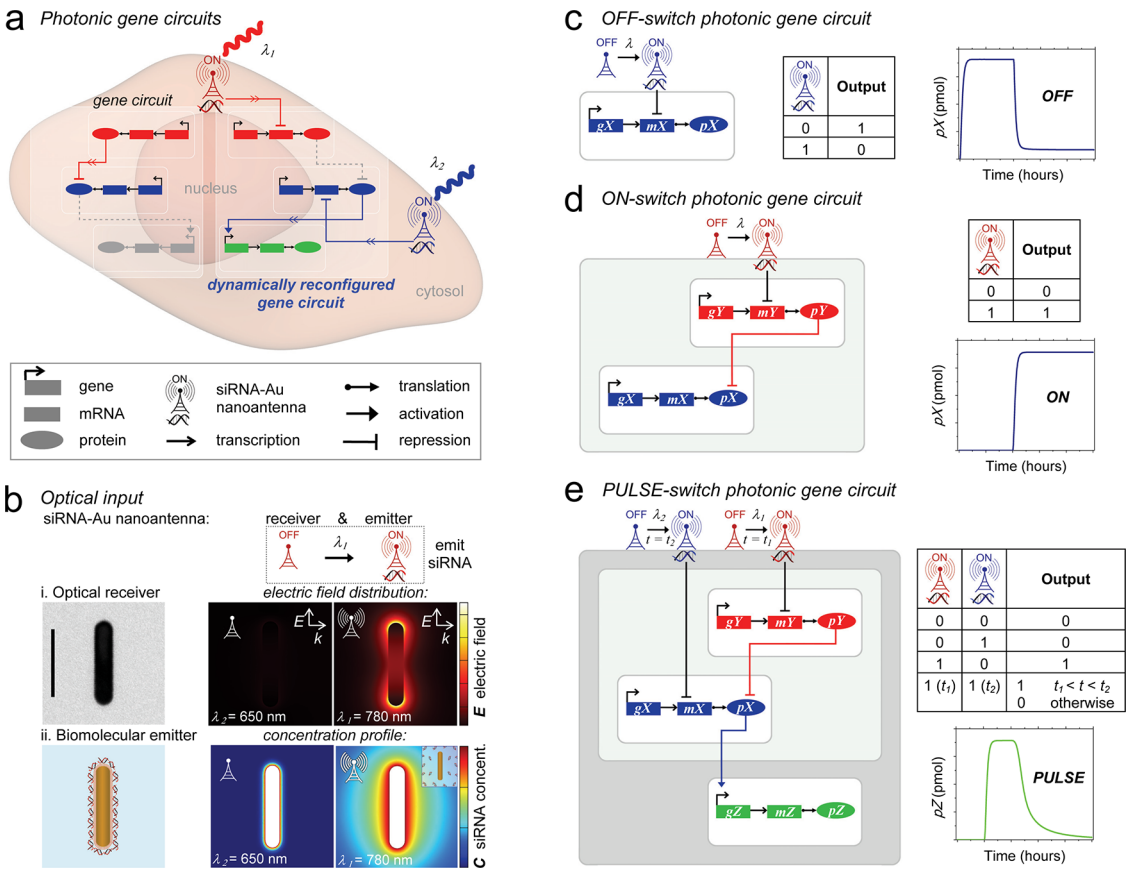

Figure 1. Photonic gene circuits. (a) Dynamic optical circuit reconfiguration is enabled by resonant siRNA-Au nanoantennas as optical inputs to existing circuit connections of living cells, forming photonic gene circuits. Legend notates symbols and circuit connections. (b) Resonant siRNA-Au nanoantennas function as selectively addressable optical receivers and biomolecular emitters of siRNA. (i) Transmission electron microscopy image of the nanoantenna structure (gold material). Scale bar is 50 nm. Electric field calculated using excitation $\lambda = 780$ nm or $\lambda = 650$ nm. Antenna effect is "on" at the resonance state and "off" at the nonresonance state of the nanoantenna. (ii) Conceptual image of siRNA-Au nanoantenna. The nanoantenna surface is modified with a cationic phospholipid bilayer, and negatively charged siRNA is adsorbed to the surface, forming the siRNA-Au nanoantenna. Calculated concentration profiles: siRNA emitted from the nanoantenna when the antenna effect is "on" at the resonance state, and no siRNA emitted when the antenna effect is "off" at the nonresonance state. Inset: Conceptual image of siRNA emission from optically addressed siRNA-Au nanoantenna. (c) Circuit diagram, logic table, and model of *OFF*-switch photonic gene circuit. (d) Circuit diagram, logic table, and model of *ON*-switch photonic gene circuit. (e) Circuit diagram, logic table, and model of *PULSE*-switch photonic gene circuit.

demonstrated by liberating interfering oligonucleotides from nanoantennas using optically generated, surface-localized heat.[4,7,8,12] However, the optical gene silencing mechanism has not yet been utilized, in the context of gene circuits, to dynamically reconfigure existing gene circuits and optically engineer new gene circuit configurations.

Here, on-demand optical circuit reconfiguration is enabled by optically addressable siRNA-Au nanoantennas functioning as optical receivers and biomolecular emitters of siRNA *via* the optical gene silencing mechanism. In this manner, siRNA-Au nanoantennas serve as optical inputs to existing circuit connections (Figure 1a), forming photonic gene circuits (Figure 1c, d, e). Photonic gene circuits are modular, allowing subcircuits to be combined on-demand. This work represents a new way to engineer functional gene circuits, as it allows, for the first time, temporally precise modulation and dynamic reconfiguration of native gene circuits.

RESULTS AND DISCUSSION

Among the different nanoantenna structures of current widespread interest, a rod-shaped Au nanoantenna (*i.e.*, Au nanorod) was selected here (Figure 1b, i) because of its large optical absorption cross-section, narrow spectral bandwidth of the longitudinal plasmon resonance band, and tunable longitudinal plasmon resonance wavelength in the near-infrared (NIR) regime, where cells are essentially transparent.[23] The optical properties of an Au nanorod are dominated by its plasmon resonance. At resonance, the optical near-field shows two regions of high-field intensity (Figure 1b, i) due to charge accumulation at each end of the nanoantenna.[24] These regions of high-field intensity indicate that the nanoantenna functions as an optical receiver to focus freely propagating optical fields down to nanometer-scale dimensions.[25] This antenna effect is prominent at the resonance state of

the nanoantenna, where the excitation wavelength is matched with the plasmon resonance wavelength. In Figure 1b, i, this antenna effect is seen to be "on" at the resonance state and "off" at the nonresonance state of a nanoantenna, where the resonance and nonresonance states depend on aspect ratio. We exploited this antenna effect to design nanoantennas, based on aspect ratios, that can be optically addressed with minimal antenna crosstalk for use in constructing photonic gene circuits.

For use as biomolecular emitters, resonant siRNA-Au nanoantennas were designed such that the photothermal heat transfer from the nanoantenna surface to the surrounding cellular environment is highly localized, decaying exponentially,[26] and therefore is thought to have minimal adverse effects on cells. To further minimize adverse effects, the plasmon resonance wavelength is also tuned to the NIR since cells are essentially transparent in the NIR regime.[23] In this work, the nanoantenna surface is modified with a cationic phospholipid bilayer,[5] and negatively charged siRNA is adsorbed to the surface. Optically generated, surface-localized heat is used to emit siRNA from the nanoantenna. The calculated temperature profiles (Figure S1) show this heat generated is highly localized to the surface and decays exponentially within 100 nm. The calculated concentration profiles in Figure 1b, ii, show siRNA is emitted from the nanoantenna when the antenna effect is "on" at the resonance state. We utilized this resulting outcome of the antenna effect to design siRNA-Au nanoantennas that can be optically addressed to emit siRNA with minimal antenna crosstalk for use in constructing photonic gene circuits.

The siRNA-Au nanoantennas were synthesized and experimentally characterized as functional optical receivers and biomolecular emitters of siRNA (further information in Methods and Figures S2−S8). Inside living cells, interfering siRNA silences intracellular genes in a sequence-specific manner, but alone, lacks the temporal control necessary for precise modulation. The siRNA-Au nanoantennas combine the benefits of sequence-specificity with spatiotemporal control.

Dark-field microscopy was used to visualize internalized siRNA-Au nanoantennas (Figure 2a). Human cervical carcinoma HeLa cells were illuminated with unpolarized white light from an oblique angle using a dark-field condenser lens, and scattered light was collected using a transmission-mode dark-field microscope. To locate cells' boundaries and nuclei, DIC images were overlaid with DAPI-stained images and placed adjacent to dark-field scattering images. Using dark-field microscopy, scattered light from individual nanoantennas can be visualized.[27,28] In Figure 2c, individual nanoantennas appear uniformly distributed in the cytosol of HeLa cells. It is clearly evident from Figure 2 that scattered light from cells containing nanoantennas (Figure 2c) is easily differentiated from cells lacking nanoantennas (Figure 2b). Long-term viability/cytotoxicity and proliferation studies were previously conducted to ensure that internalized nanoantennas[5] and optical excitation[4] caused no adverse effects on cell behavior.

The circuit diagram for an *OFF*-switch photonic gene circuit is shown in Figure 2d, i. Gene *X* (*gX*) is transcribed into mRNA *X* (*mX*), which is then translated into protein *X* (*pX*). The siRNA-Au nanoantenna is introduced into the circuit diagram as an optical input. Circuit connections are notated in the legend in Figure 1a. When the siRNA-Au nanoantenna is optically addressed, siRNA targeting *X* is emitted from the siRNA-Au nanoantenna, thereby turning off *mX* and subsequently *pX* due to optical gene silencing of *X* (Figure S9). To experimentally demonstrate the *OFF*-switch circuit in HeLa cells, the activated isoform nuclear factor κB-p65 (p65) was chosen to represent *X*, and flow cytometric analysis was used to quantify the *OFF*-switch of p65 (*i.e.*, decrease in p65 protein levels) in single HeLa cells. In Figure 2d, p65 protein levels decreased by $\Delta = 40\%$ as a result of the *OFF*-switch photonic gene circuit. No decrease in p65 protein levels was observed when optically addressed, nonresonant siRNA-Au nanoantennas failed to emit p65 siRNA (Figure 2d, ii). No decrease in p65 protein levels were observed when optically addressed siRNA-Au nanoantennas emitted scrambled siRNA (Figure 2d, iii). It was observed in the positive control (Figure S10a) that siRNA alone targeting p65 decreased protein expression levels by 60%. We surmise that the difference between optical gene silencing and the positive control could be due to the efficiency of siRNA escaping out of endosomes and into the cytosol after photothermal destabilization of the endosomal membrane. Future in-depth imaging studies of photothermal destabilization of endosomal membranes should help to better understand and improve efficiencies of siRNA escape from photothermally destabilized endosomes. A logic table summarizing the *OFF*-switch behavior is shown in Figure 2e, where "0" (off-state) and "1" (on-state) represent low and high concentrations, respectively. In Figure 2e, HeLa cells immunostained for p65 showed an overall high fluorescence when the input was "0" and an overall low fluorescence when the input was "1" (optically addressed *OFF*-switch). *OFF*-switch photonic gene circuits presented in Figure 2 are not limited to p65 and can be constructed for virtually any protein of interest. *OFF*-switch photonic gene circuits are also modular and can be combined with other naturally occurring subcircuits and/or other photonic subcircuits.

We take advantage of this modularity to construct an *ON*-switch photonic gene circuit. In the circuit diagram in Figure 3b, genes (*gX*, *gY*) are transcribed into mRNA (*mX*, *mY*) and are then translated into proteins (*pX*, *pY*), where *pY* inhibits the active form of *pX*, represented by pX_{nuc}, by sequestering pX_{nuc} in the

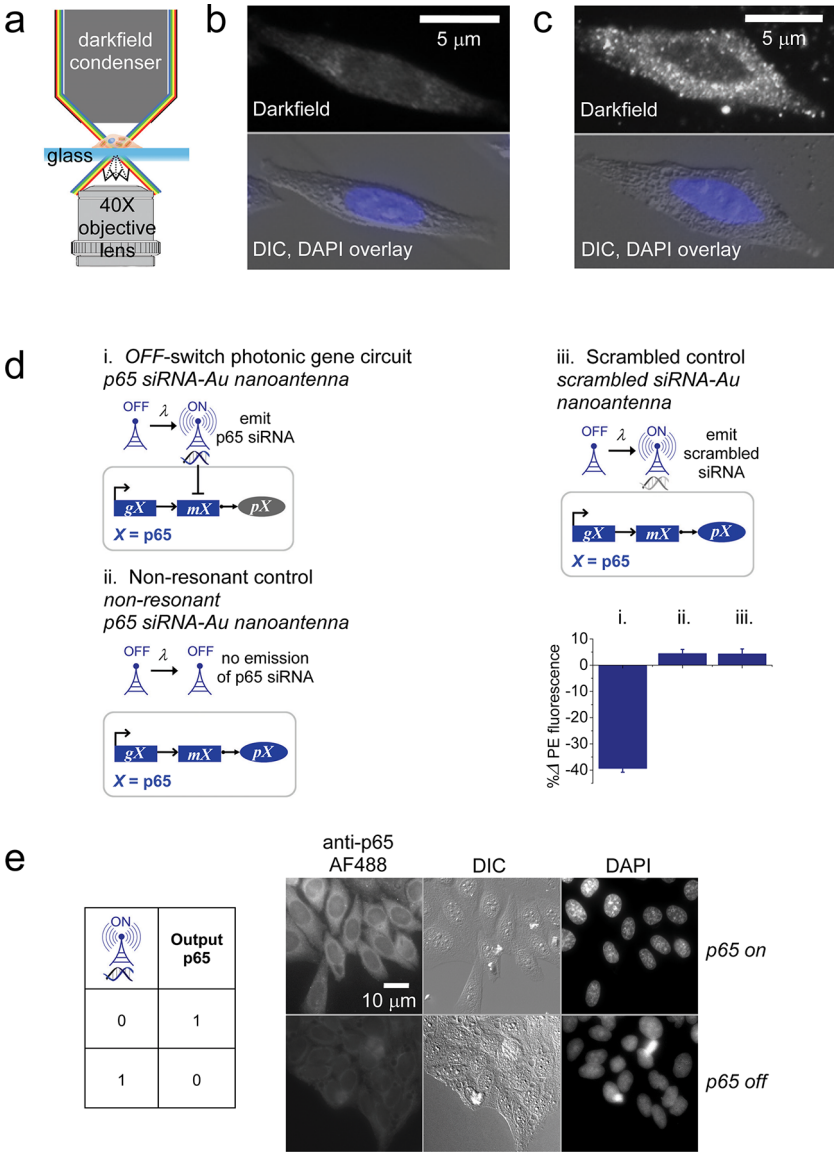

Figure 2. *OFF*-switch photonic gene circuit. (a) Schematic of microscope setup to visualize internalized siRNA-Au nanoantennas in HeLa cells. (b) Dark-field scattering images of HeLa cells lacking nanoantennas (control). DAPI-stained nuclei images overlaid with DIC images. (c) Dark-field scattering images of HeLa cells with internalized nanoantennas. DAPI-stained nuclei images overlaid with DIC images. (d) Flow cytometric analysis of p65 *OFF*-switch photonic gene circuit in single HeLa cells. HeLa cells immunostained using phycoerythrin (PE)-labeled anti-p65. Flow cytometric data expressed as percent change of mean PE fluorescence intensity between experiment and reference cells (further information in Figure S10) for *OFF*-switch photonic gene circuit, nonresonant control, and scrambled control. (i) Circuit diagram for p65 *OFF*-switch photonic gene circuit. (ii) Circuit diagram for nonresonant control. (iii) Circuit diagram for scrambled control. (e) Logic table for *OFF*-switch photonic gene circuit. Immunofluorescence imaging of p65 *OFF*-switch photonic gene circuit in HeLa cells: DIC, anti-p65-AF488 immunostaining of p65, and DAPI staining of nuclei.

cytoplasm (off-state). To construct an *ON*-switch of pX_{nuc}, a modular *OFF*-switch subcircuit is introduced into this circuit diagram to generate a double-negative signal (*i.e.*, inhibit the inhibitor *pY*). Therefore, when the siRNA-Au nanoantenna is optically addressed, *pY* is turned off, thereby enabling pX_{nuc} to turn on and freely translocate to the nucleus (on-state). To experimentally demonstrate this *ON*-switch circuit configuration in HeLa cells, p65 was chosen to represent *X* and the inhibitor κB (IκB) was selected to represent *Y*. First, flow cytometric analysis was used to quantify the IκB *OFF*-switch subcircuit (*i.e.*, decrease in IκB protein levels) in single HeLa cells. In Figure 3a, IκB protein levels decreased by Δ = 40% as a result of the *OFF*-switch subcircuit. Having confirmed the IκB *OFF*-switch subcircuit, the *ON*-switch of $p65_{nuc}$ was studied using immunofluorescence imaging. A logic table summarizing the *ON*-switch behavior is shown in Figure 3b. In the off-state, IκB and p65 form an inactive complex such that p65 is sequestered in the cytoplasm. Therefore, HeLa cells immunostained for p65 showed an overall low fluorescence in the nucleus when the input was "0". Conversely, cells showed a strong nuclear presence of p65 ($p65_{nuc}$) when the input was "1"

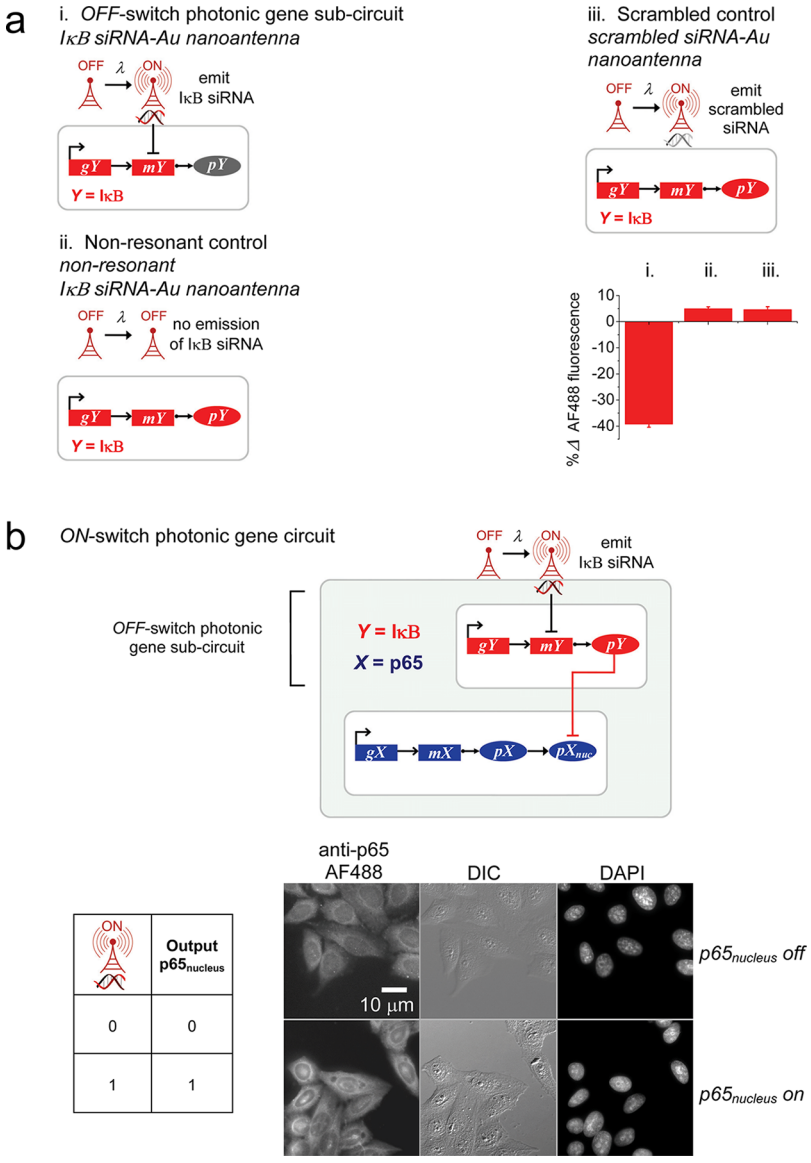

Figure 3. *ON*-switch photonic gene circuit. *ON*-switch photonic gene circuit is constructed using a modular *OFF*-switch subcircuit. IκB and p65 were chosen to represent *Y* and *X*, respectively. (a) Flow cytometric analysis of IκB *OFF*-switch subcircuit in single HeLa cells. HeLa cells immunostained using AF488 -labeled anti-IκB. Flow cytometric data expressed as percent change of mean AF488 fluorescence intensity between experiment and reference cells (further information in Figure S11) for IκB *OFF*-switch subcircuit, nonresonant control, and scrambled control. (i) Circuit diagram for IκB *OFF*-switch subcircuit. (ii) Circuit diagram for nonresonant control. (iii) Circuit diagram for scrambled control. (b) Logic table for *ON*-switch photonic gene circuit. In the on-state, p65 translocates to the nucleus ($p65_{nucleus}$). Immunofluorescence imaging of *ON*-switch photonic gene circuit in HeLa cells: DIC, anti-p65-AF488 immunostaining of p65, and DAPI staining of nuclei.

(optically addressed *ON*-switch). To locate cells' boundaries and nuclei, DIC images and DAPI images were placed adjacent to p65 immunostained images. Similar to *OFF*-switch circuits, *ON*-switch photonic gene circuits are also modular and can potentially be combined with multiple subcircuits to construct more sophisticated photonic gene circuits.

To construct more sophisticated photonic gene circuits from multiple subcircuits, modular subcircuits should function independently of each other. This can be accomplished with siRNA-Au nanoantennas that operate at distinct optical wavelengths (Figure 4b), based on aspect ratio (AR), with minimal antenna crosstalk. Selective optical release of two distinct DNA strands has been previously demonstrated,[15] but not yet in the context of engineering gene circuits. Fluorescence analysis was conducted to measure antenna crosstalk between 4.0 AR and 2.5 AR siRNA-Au nanoantennas. Using λ_1 = 785 nm, a statistically significant increase in fluorescence intensity was seen when optically addressed resonant siRNA-Au nanoantennas (4.0 AR) emitted fluorescently labeled siRNA, while no increase in fluorescence intensity was observed when nonresonant nanoantennas (2.5 AR) were optically addressed (Figure 4b, Figure S6a), indicating no antenna crosstalk using λ_1 = 785 nm. It was observed that when using λ_2 = 660 nm (Figure S6b), a statistically significant increase in the fluorescent

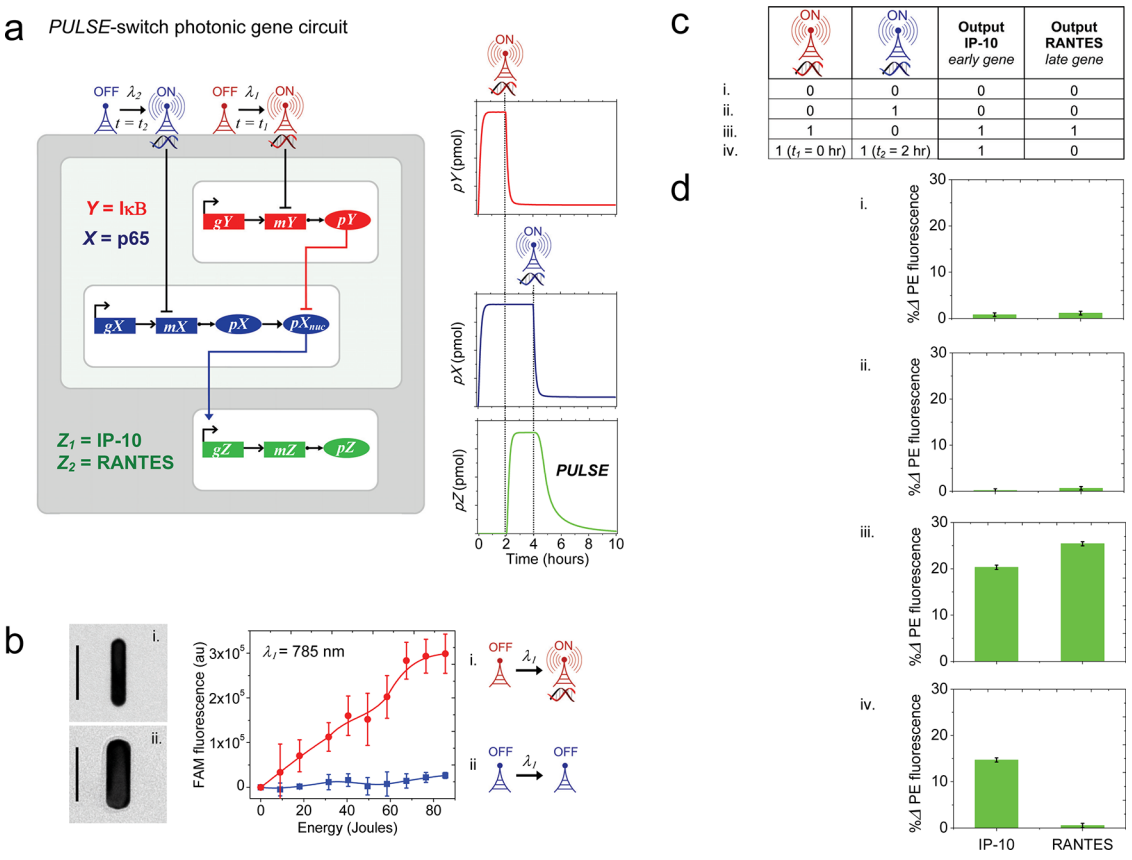

Figure 4. *PULSE*-switch photonic gene circuit. (a) A *PULSE*-switch photonic gene circuit is constructed using multiple, independently operating subcircuits. Circuit diagram and model for *PULSE*-switch photonic gene circuit. The *ON*-switch subcircuit functions to initiate the pulse of target protein *pZ* at time t_1. In this *ON*-switch subcircuit, siRNA-Au nanoantennas (4.0 AR) are optically addressed at time t_1 using $\lambda_1 = 785$ nm. The *OFF*-switch subcircuit then operates to terminate the pulse of target *pZ* at time t_2. In this *OFF*-switch subcircuit, siRNA-Au nanoantennas (2.5 AR) are optically addressed at time t_2 using $\lambda_2 = 660$ nm. IκB and p65 were chosen to represent *Y* and *X*, respectively. Two targets, IP-10 and RANTES, were selected to represent *Z* (as Z_1 and Z_2, respectively). (b) Photonic gene subcircuits operate independently of each other using optically addressable siRNA-Au nanoantennas with minimal antenna crosstalk. Fluorescence analysis of fluorescently labeled siRNA emitted from optically addressed resonant siRNA-Au nanoantennas (further information in Figure S6). (i) Transmission electron microscopy image of the 4.0 AR nanoantenna structure (gold material). (ii) Transmission electron microscopy image of the 2.5 AR nanoantenna structure (gold material). Scale bar is 50 nm. (c) Logic table for 2 h *PULSE*-switch photonic gene circuit. (d) Flow cytometric analysis of 2 h *PULSE*-switch photonic gene circuit in single HeLa cells corresponding to logic table. HeLa cells immunostained using phycoerythrin (PE)-labeled anti-IP-10 or PE-labeled anti-RANTES. Flow cytometric data expressed as percent change of the mean PE fluorescence intensity between experiment (conditions listed in logic table) and reference cells (further information in Figure S12).

intensity was seen with resonant nanoantennas (2.5 AR), and a small but measurable increase in fluorescent intensity was also observed with nonresonant nanoantennas (4.0 AR). In this case, signal interference occurred with nonresonant nanoantennas, but this can be circumvented in the future by designing nanoantennas to achieve a wider spectral separation between their longitudinal plasmon resonance bands.

Having confirmed that siRNA-Au nanoantennas can selectively receive optical signals and preferentially emit siRNA with minimal antenna crosstalk, we constructed a *PULSE*-switch photonic gene circuit from multiple, independently operating subcircuits. In the circuit diagram in Figure 4a, *ON*-switch and *OFF*-switch subcircuits are combined to form a *PULSE*-switch circuit. The *ON*-switch subcircuit functions to initiate the pulse of target protein *pZ* at time t_1. In this *ON*-switch subcircuit, siRNA-Au nanoantennas (4.0 AR) are optically addressed at time t_1 using $\lambda_1 = 785$ nm to emit siRNA targeting *Y*. This causes *pY* to turn off, pX_{nuc} to turn on, and subsequently target *pZ* to turn on. The *OFF*-switch subcircuit then operates to terminate the pulse of target *pZ* at time t_2. In this *OFF*-switch subcircuit, siRNA-Au nanoantennas (2.5 AR) are optically addressed at time t_2 using $\lambda_2 = 660$ nm to emit siRNA targeting *X*. This causes *pX* to turn off and subsequently target *pZ* to turn off. *ON*-switch and *OFF*-switch subcircuits should operate separately, with minimal signal interference from the other circuit. However, since some signal interference was observed with $\lambda_2 = 660$ nm (Figure S6b) while no signal interference was observed with $\lambda_1 = 785$ nm, here, the order of operation became critical. The *ON*-switch was first designed to operate at $\lambda_1 = 785$ nm since no signal interference

occurred using λ_1 = 785 nm (Figures 4b and S6a). The *OFF*-switch was then designed to operate at λ_2 = 660 nm. In this order of operation, both circuits were able to operate independently of each other. In future versions, signal interference will be minimized by designing nanoantennas with a wider spectral separation between their longitudinal plasmon resonance bands or by designing new geometries of nanoantennas with narrower spectral bandwidths.

To experimentally demonstrate this *PULSE*-switch photonic gene circuit in HeLa cells, IκB and p65 were chosen to represent *Y* and *X*, respectively. To test the kinetic behavior of the *PULSE*-switch photonic gene circuit, temporally regulated genes were used as a functional assay of kinetics. Two NF-κB regulated genes (IP-10 and RANTES) that display different transcriptional activation profiles were selected to represent *Z* (as Z_1 and Z_2, respectively). IP-10, an early response gene, is known to be immediately activated within 30 min of stimulation,[29] whereas RANTES, a late response gene, requires more than 3 h of stimulation to turn on.[30] We used these two temporally regulated genes to functionally validate the 2 h *PULSE*-switch shown in Figure 4a. We reasoned that if a 2 h *PULSE*-switch was constructed, IP-10 should turn on while RANTES should remain off. To implement the 2 h *PULSE*-switch, we constructed a logic table for IP-10 and RANTES summarizing four possible conditions (Figure 4c). These conditions listed in the logic table were shown to function correctly using flow cytometric analysis of IP-10 and RANTES (Figure 4d). Notably, Figure 4d, iv, confirmed that IP-10 is turned on while RANTES is turned off as a result of the 2 h *PULSE*-switch. In addition to functional assays of kinetics, visual assays using fluorescently labeled proteins can also be utilized in the future to characterize photonic gene circuits.

In this work, we have demonstrated the construction of a *PULSE*-switch circuit using two independent subcircuits. This was accomplished with two independently operating nanoantennas. In the future, more sophisticated circuit configurations can be conceivably constructed by combining multiple, independent subcircuits. Due to the narrow spectral bandwidths of Au nanorods, four subcircuits could potentially operate independently of each other in the visible and near-infrared wavelength regimes. More subcircuits could potentially be combined by synthesizing new geometries of nanoantennas with more narrow spectral bandwidths in the visible and near-infrared wavelength regimes. As more subcircuits are combined, signal strength should be addressed to improve circuit performance. Signal distortions, such as amplitude reductions, occur due to inherent dilution, degradation, and diffusion effects in the intracellular environment. These signal distortions inherently occur in native gene circuits. Inevitably, photonic gene circuits are subject to similar signal distortions as native gene circuits. Improving RNA interference efficiency could help to overcome the effects of signal amplitude reduction. For example, designing siRNA to bind to optimal target sites could help to improve RNA interference efficiency. Incorporating other geometries of RNA, such as hairpin-shaped or dumbbell-shaped RNA, with nanoantennas, which may be less prone to degradation, could also help to improve RNA interference efficiency in the intracellular environment.

CONCLUSIONS

In closing, we have demonstrated the construction of photonic gene circuits using optically addressable siRNA-Au nanoantennas in living cells. Photonic gene circuits are a promising approach to systematically study native gene circuits in complex, naturally occurring living systems. Since native gene circuits remain genomically unaltered, photonic gene circuits are a promising alternative to synthetic circuits for studying temporal dynamics[31] in native gene circuits. Toward *in vivo* applications, we envision constructing photonic gene circuits using optically addressable siRNA-Au nanoantennas in optically transparent whole model organisms, such as *Caenorhabditis elegans* and zebrafish embryos, to study temporal dynamics and to probe, identify, and reconfigure malfunctioning gene circuits as a therapeutic strategy. We envision that light also could be delivered transdermally or by fiber optics in other model organisms that are not optically transparent. We believe photonic gene circuits could play a pivotal role in engineering functional gene circuits as they enable, for the first time, dynamic reconfiguration and temporally precise modulation of native gene circuits.

METHODS

Modeling of Optical Receiver. The finite element method (COMSOL Multiphysics software) was used to model a 3-D Au nanorod (4.0 and 2.5 AR) suspended in water and to achieve a solution to the Helmholtz wave equation: $\nabla \times (\mu_r^{-1} \nabla \times E) - k_0^2(\varepsilon_r - j\sigma\omega\varepsilon_0)E = 0$. The Au nanorod was constructed using a cylinder with hemispheres on each end of the cylinder. The relative permeability of Au was assumed to be $\mu_r = 1$, and the complex permittivity of Au ε_r was assumed to be a function of wavelength λ. A spherical perfectly matched layer and an integration layer, modeled by concentric spheres, were used to reach perfect absorption at the outer boundary and minimize spurious reflections. A plane wave was used for excitation (λ = 780 nm or λ = 650 nm). The adaptive mesh was refined until the maximum electric field converged.

Modeling of Optically Generated Surface Localized Heat. We solved the bioheat transfer equation: $\rho C(\partial T/\partial t) + \nabla \cdot (-k\nabla T) = \rho_b C_b \omega_b (T_b - T) + Q_{met} + Q_{ext}$. Time-average resistive heat (W/m^3) was used for the spatial heat source Q_{ext} under the assumption that electromagnetic energy was converted to heat by resistive heating. The thermal conductivity of gold, density of gold, and specific heat of gold were assumed to be k_g = 320 W/m-K,

ρ_g = 19 300 kg/m^3, and C_g = 129 J/kg-K, respectively.[32,33] The thermal conductivity of water, density of water, and specific heat of water were assumed to be k_w = 0.61 W/m-K, ρ_w = 1000 kg/m^3, and C_w = 42000 J/kg-K, respectively. The metabolic heat source Q_{met} and the perfusion rate ω_b were assumed to be insignificant.

Modeling of Biomolecular Emitter. To investigate biomolecular emission of siRNA, we solved the thermal diffusion equation: $\partial c/\partial t = \nabla \cdot [D\nabla c + D_T c \nabla T]$. Electromagnetic energy was assumed to be converted to surface-localized heat and was used here for temperature T. It was assumed that siRNA dissociated from the surface of the nanoantenna at elevated temperatures, and mass flux occurred due to the temperature gradient in addition to the siRNA concentration gradient. The diffusion coefficient and the thermal diffusion coefficient of siRNA were estimated to be $D = 36.00 \times 10^8$ cm^2/s and $D_T = 0.45 \times 10^8$ cm^2/s-K, respectively, based on double-stranded DNA of similar length.[34] Using the surface density (9.0×10^{12} molecules/cm^2) and the size dimensions, the initial concentrations of siRNA were calculated to be $c_0 = 1.81 \times 10^{-14}$ mol/m^3 for 4.0 AR nanoantennas and $c_0 = 2.11 \times 10^{-14}$ mol/m^3 for 2.5 AR nanoantennas, respectively.

Modeling of Photonic *OFF*-Switch, *ON*-Switch, and *PULSE*-Switch Gene Circuits. The *OFF*-switch (eqs 1−3), *ON*-switch (eqs 4−8), and *PULSE*-switch (eqs 9−17) circuit configurations were modeled (Matlab software). Genes (*gX, gY, gZ*) were transcribed into mRNA (*mX, mY, mZ*), which were then translated into proteins (*pX, pY, pZ*), where *gX, gY, gZ, mX, mY, mZ, pX, pY, and pZ* denote concentrations. Degradation of messenger mRNA by optical gene silencing using gold nanoantennas functionalized with siRNA (*NAsirna1*, *NAsirna2*) were modeled based on Michaelis−Menten/Hill kinetics.

OFF-Switch Circuit

$$\frac{dmX}{dt} = k_{X1} \cdot gX - k_{d\_mX} \cdot mX - k_{d\_sirna2\_mrna} \cdot \beta_X \cdot \left(\frac{NA_{on}sirna2}{K_x + NA_{on}sirna2}\right) \cdot mX \quad (1)$$

$$\frac{dpX}{dt} = k_{X2} \cdot mX - k_{d\_pX} \cdot pX \quad (2)$$

$$\frac{dNA_{on}sirna2}{dt} = k_{L2} * NAsirna2 - k_{d\_sirna2} * NA_{on}sirna2 \quad (3)$$

ON-Switch Circuit

$$\frac{dmY}{dt} = k_{Y1} \cdot gY - k_{d\_mY} \cdot mY - k_{d\_sirna1\_mrna} \cdot \beta_Y \cdot \left(\frac{NA_{on}sirna1}{K_Y + NA_{on}sirna1}\right) \cdot mY \quad (4)$$

$$\frac{dmX}{dt} = k_{X1} \cdot gX - k_{d\_mX} \cdot mX \quad (5)$$

$$\frac{dpX}{dt} = k_{X2} \cdot mX - k_{d\_pX} \cdot pX \quad (6)$$

$$\frac{dpX_{nuc}}{dt} = k_{X3} \cdot pX - k_{d\_pXnuc} \cdot pX_{nuc} - k_{d\_pXnuc\_pY} \cdot pY \cdot pX_{nuc} \quad (7)$$

$$\frac{dNA_{on}sirna1}{dt} = k_{L1} * NAsirna1 - k_{d\_sirna1} * NA_{on}sirna1 \quad (8)$$

PULSE-Switch Circuit

$$\frac{dmY}{dt} = k_{Y1} \cdot gY - k_{d\_mY} \cdot mY - k_{d\_sirna1\_mrna} \cdot \beta_Y \cdot \left(\frac{NA_{on}sirna1}{K_Y + NA_{on}sirna1}\right) \cdot mY \quad (9)$$

$$\frac{dpY}{dt} = k_{Y2} \cdot mY - k_{d\_pY} \cdot pY \quad (10)$$

$$\frac{dmX}{dt} = k_{X1} \cdot gX - k_{d\_mX} \cdot mX - k_{d\_sirna2\_mrna} \cdot \beta_X \cdot \left(\frac{NA_{on}sirna2}{K_x + NA_{on}sirna2}\right) \cdot mX \quad (11)$$

$$\frac{dpX}{dt} = k_{X2} \cdot mX - k_{d\_pX} \cdot pX \quad (12)$$

$$\frac{dpX_{nuc}}{dt} = k_{X3} \cdot pX - k_{d\_pXnuc} \cdot pX_{nuc} - k_{d\_pXnuc\_pY} \cdot pY \cdot pX_{nuc} \quad (13)$$

$$\frac{dmZ}{dt} = k_{Z1} * gZ * \beta_Z * \left(\frac{pX_{nuc}{}^n}{K_Z + pX_{nuc}{}^n}\right) - k_{d\_mZ} * mZ \quad (14)$$

$$\frac{dpZ}{dt} = k_{Z2} * mZ - k_{d\_pZ} * pZ \quad (15)$$

$$\frac{dNA_{on}sirna1}{dt} = k_{L1} * NAsirna1 - k_{d\_sirna1} * NA_{on}sirna1 \quad (16)$$

$$\frac{dNA_{on}sirna2}{dt} = k_{L2} * NAsirna2 - k_{d\_sirna2} * NA_{on}sirna2 \quad (17)$$

Kinetic rates and initial values are listed in Supporting Information Table 1 and were approximated similarly to those previously reported in the literature for a eukaryotic model.[35] It was assumed that no siRNA was emitted by nonresonant siRNA-Au nanoantennas. It was also assumed that when siRNA-Au nanoantennas were optically addressed with the correct optical wavelength, all siRNA was emitted. Since the model's time scale was on the order of hours, it was assumed that nanoantennas did not degrade in this time frame, and therefore the concentration of nanoantennas remained the same. Due to the tight packing of siRNA on the nanoantennas, steric hindrances inhibited nuclease degradation[36] of siRNA while siRNA was bound to the nanoantennas. Once siRNA was emitted from nanoantennas, the siRNA degraded with degradation rates as reported previously.[37]

Synthesis of RNase-Free Gold Rod-Shaped Nanoantennas. Gold nanorods of aspect ratios 2.5 and 4.0 (Figure S2) were synthesized by adapting a seed-mediated growth method[38,39] to an RNase-free environment.[5] All solutions were prepared using 0.2 μm filtered DEPC-treated water. All glassware and metalware were baked at 240 °C for 24 h to remove exogenous RNases. All pipetting devices and counter space was treated with 70% ethanol. All disposable plastic pipet tips and centrifuge tubes were certified to be free of RNase. The resultant CTAB-coated gold nanoantennas were ensured to be free of RNases by detecting RNase activity over time (Figure S3). RNase activity in the supernatant solution was detected using an RNase activity kit (Ambion) and was quantitatively measured over time using a fluorometer (Fluoromax-3, Horiba Jobin Yvon). The concentration of CTAB-coated nanorods was confirmed by adjusting to an absorbance of 1 at the longitudinal plasmon resonance wavelength using UV−vis spectroscopy (8453, Hewlett-Packard). Aspect ratios were determined by scanning electron microscopy and transmission electron microscopy.

Synthesis of siRNA-Au Nanoantennas. Gold nanoantennas functionalized with siRNA were synthesized as previously described.[5] In summary, the CTAB surfactant on the nanoantennas' surface was exchanged with a cationic phospholipid bilayer to form biologically functional cationic phospholipid−gold nanoantennas. To remove excess CTAB surfactant, 500 μL of unmodified CTAB-coated nanoantennas (UV−vis absorbance of 1) was centrifuged at 5000 rpm for 10 min. A 10 μL pellet was transferred to a new microcentrifuge tube, redispersed in 500 μL of nuclease-free water, briefly vortexed, and sonicated for 1 min. To replace CTAB surfactant with a phospholipid bilayer membrane at the nanoantenna surface, nanoantennas were then centrifuged again at 5000 rpm for 10 min. A 10 μL pellet was

transferred to a new microcentrifuge tube, resuspended in 50 μL of Oligofectamine, briefly vortexed, and sonicated for 1 min.

After the CTAB coating was replaced with a cationic phospholipid coating, siRNA was then conjugated to the nanoantennas. IκB siRNA (Qiagen) was conjugated to nanoantennas (4.0 AR), and p65 siRNA (Qiagen) was conjugated to nanoantennas (2.5 AR). To 500 μL of nanoantenna solution, 2 μL of 100 μM siRNA was added. The solution was vortexed and allowed to incubate for 30 min. To remove excess siRNA from solution, nanoantennas were washed with nuclease-free water by centrifugation at 5000 rpm for 10 min and finally resuspended in 500 μL of nuclease-free water. After preparation of siRNA-Au nanoantennas, an absorbance of 0.2 was measured by UV−vis (8453, Hewlett-Packard). By comparing with the original nanoantennas' UV−vis absorbance of 1, the concentration of siRNA-Au nanoantennas was estimated to be approximately one-fifth the original concentration (approximately 6 μg/mL or 1.4×10^{11} nanoantennas/mL).

For internalization, the siRNA-Au nanoantennas were then coated with cationic phospholipids to improve entry into living cells. First, 1000 μL of siRNA-Au nanoantennas was concentrated into a 10 μL pellet by centrifugation at 5000 rpm for 20 min. The pellet was transferred to a new microcentrifuge tube and then resuspended in 25 μL of Oligofectamine. The solution was vortexed and allowed to incubate for 20 min. For higher concentrations of conjugates, the multiple tubes of conjugates were prepared the same as described above. After 20 min, 175 μL of nuclease-free water was added to each tube to dilute the concentration of free cationic phospholipids in solution. The conjugates were concentrated into a 0.5 μL pellet by centrifugation for internalization.

Thermal Liberation of siRNA from siRNA-Au Nanoantennas. Prior to optically addressing siRNA-Au nanoantennas, the controlled thermal liberation of siRNA from the surface was first demonstrated. If siRNA dissociates from the cationic phospholipid bilayer at elevated temperatures, this unbinding event should change the dielectric constant of the medium locally surrounding the nanoantennas and therefore result in an observable shift in the nanoantennas' longitudinal plasmon resonance wavelength.[40,41]

A UV−vis spectrometer containing a thermal-jacketed cell was used to evaluate the temperature-dependent absorbance of the nanoantenna-containing solutions. To each separate cell of an eight-cell micro sample holder (208-92086, Shimadzhu) was added 50 μL of siRNA-Au nanoantennas or unconjugated nanoantennas. Samples were simultaneously heated from 20 to 70 °C (10 °C increment, 5 min) using a temperature-controlled UV−vis spectrometer (2501, Shimadzhu). Absorbance spectra were collected for each sample at each temperature increment.

Control nanoantennas lacking siRNA cargo showed no shift in the longitudinal plasmon resonance wavelength at elevated temperatures (Figure S4b), indicating that the phospholipid bilayer remained stable at elevated temperatures. In contrast, siRNA-Au nanoantenna conjugates showed a marked blue-shift in the longitudinal plasmon resonance wavelength at elevated temperatures due to the dissociation of siRNA from the surface (Figure S4a). Additionally, supplemental Figure S4c shows that the longitudinal plasmon resonance wavelength of the siRNA-Au nanoantennas blue-shifts with incrementing temperature until it eventually matches the longitudinal plasmon resonance wavelength of the control nanoantennas, strongly suggesting the complete dissociation of siRNA from the intact phospholipid bilayer at 70 °C.

Optical Setup. An 80 mW 785 nm CW diode laser (Newport Corp.) and a 60 mW 660 nm CW diode laser (Newport Corp.) were optically coaligned such that their beams simultaneously overlapped (Figure S5). First, both lasers were positioned parallel to each other on a manually adjustable *xyz* stage. A dichroic mirror (Omega Optical) was positioned below the 785 nm laser. A mirror (Omega Optical) was placed below the 660 nm laser. To make the two beams orthogonal to each other, the 660 nm laser beam was reflected 90° toward the direction of the other laser by the mirror. The dichroic mirror transmitted the 785 nm laser beam and reflected the 660 nm laser beam another 90° such that both beams simultaneously overlapped and coaligned with each other. To circularly polarize the light, an achromatic quarter-wave plate (CVI Laser Corp.) was placed below the coaligned beams.

Emission of siRNA from Optically Addressed siRNA-Au Nanoantennas. Having established that siRNA can be thermally dissociated from the cationic phospholipid bilayer, siRNA-Au nanoantennas of different aspect ratios were then selectively addressed. Because their narrow longitudinal plasmon resonance bands are spectrally separated (Figure S2a), rod-shaped Au nanoantennas can be optically addressed to selectively emit siRNA.

6-Carboxyfluorescein (FAM; excitation 495 nm, emission 520 nm)-labeled siRNA was bound to the nanoantennas, and unbound FAM-siRNA was then removed from the background solution by centrifugation. To a 2 mm path length quartz cuvette (3−2.45-Q-2, Starna Cells Inc.) were added 50 μL of FAM-siRNA-Au nanoantennas (2.5 AR) or FAM-siRNA-Au nanoantennas (4.0 AR). Using the optical setup shown in Figure S5, samples were illuminated from the top with 50 mW of either 785 or 660 nm light with a spot size of 2 mm. During illumination, fluorescence emission spectra were collected at 2 min intervals for each sample using a fluorometer (Fluoromax-3, Horiba Jobin Yvon). A short-pass filter was positioned in front of the fluorometer's detector to block the detector from the laser sources.

Concentration Calibration of Optically Liberated siRNA. To calibrate the fluorescent intensity to the concentration of siRNA liberated from nanoantenna carriers into solution, the fluorescent intensities of known concentrations of FAM-siRNA were also measured (Figure S7). As seen in supporting Figure S7, nanoantennas (concentration 1×10^{11} nanoantennas/mL based on UV−vis measurements) released approximately 0.05 μM siRNA after illumination. As a positive control, Triton X-100 detergent was used to disrupt the cationic phospholipid bilayer around the nanoantennas, thereby ensuring the complete liberation of all bound siRNA from nanoantennas into solution. The concentration of siRNA released using Triton X-100 matched closely the concentration of optically liberated siRNA, strongly suggesting complete liberation of siRNA from optically addressed nanoantennas.

Cell Preparation. The human cervical carcinoma cell line HeLa was purchased from the American Type Culture Collection (ATCC). Dulbecco's modified Eagle's media (DMEM) formulated with high glucose and GlutaMAX was purchased from Invitrogen and was supplemented with 10% heat-inactivated fetal bovine serum. Cells were seeded at an initial concentration of 20 000 cells/well in a 96-well plate, cultured in the supplemented media, and maintained in a 37 °C incubator with 5% CO_2 humidified air.

Visualization of Internalized siRNA-Au Nanoantennas in HeLa Cells. siRNA-Au nanoantennas were internalized into HeLa human cervical cancer cells. For visualization purposes, HeLa cells were seeded onto 12 mm gridded glass coverslips (Electron Microscopy Sciences) at 30 000 cells/well in a 24-well plate for 24 h before use. HeLa cells were then washed once with Optimem media. The 0.5 μL concentrated pellet of siRNA-Au nanoantennas was resuspended in 100 μL of Optimem media, gently mixed, and added to each well of the 24-well plate. The cells were allowed to incubate for 4 h at 37 °C. Cells were then fixed by incubating cells with 2% paraformaldehyde (Electron Microscopy Sciences) in 1× PBS per well for 10 min. Cell nuclei were stained with DAPI (Invitrogen) by incubating cells in 300 nM DAPI in 1× PBS per well for 5 min. 1× PBS was used to twice wash the cells. The coverslip containing fixed, adhered cells was then placed face down and adhered to a microscope slide. Cells were located using the grids imprinted on the coverslips.

Dark-field microscopy was used to visualize internalized siRNA-Au nanoantennas (Figure 2a). Dark-field scattering was visualized using an inverted microscope (Axiovert, Zeiss) at 40× magnification. Broadband white light was shone onto the adhered cells from an oblique angle using a dark-field condenser lens. The scattered light alone was collected using a microscope objective lens with a numerical aperture (NA) of 0.65, which was smaller than the NA (1.2−1.4) of the illumination condenser lens. To locate cells' boundaries and nuclei, DIC images were overlaid with DAPI-stained images and placed adjacent to dark-field scattering images. DIC and DAPI were

visualized using an upright fluorescence microscope (Axio Imager, Zeiss) at 40× magnification.

Concentration Characterization of Internalized siRNA-Au Nanoantennas in HeLa Cells. To estimate the amount of siRNA liberated from nanoantennas into the intracellular space, fluorescently labeled FAM-siRNA was bound to nanoantennas and unbound FAM-siRNA was then removed from the background solution by centrifugation. Known concentrations of FAM-siRNA-Au nanoantennas (7×10^{11}, 4×10^{11}, and 3×10^{11} nanoantennas/mL based on UV−vis measurements) were internalized in HeLa cells. Fluorescent intensities of individual cells were then measured by flow cytometry, and a standard concentration curve of internalized FAM-siRNA-Au nanoantennas was constructed (Figure S8b). Fluorescence quenching by nanoantennas was not observed.[5] To correlate the fluorescent intensities to FAM-siRNA concentration, control cells were incubated with known concentrations of FAM-siRNA (50, 100, and 200 nM) for 5 h. A standard concentration curve of internalized FAM-siRNA was then constructed based on flow cytometry analysis (Figure S8a). These standard curves were utilized to estimate the concentration of siRNA-Au nanoantennas necessary for optical gene silencing.

***OFF*-Switch Photonic Gene Circuit (p65 off).** HeLa cells were then washed once with Optimem media. A 0.5 μL concentrated pellet of siRNA-Au nanoantennas (2.5 AR) functionalized with p65 siRNA was resuspended in 100 μL of Optimem media, gently mixed, and added to each well of the 96-well plate. The cells were allowed to incubate for 4 h at 37 °C. After internalization of siRNA-Au nanoantennas for 4 h, the media was replaced with fresh supplemented DMEM culture media. The 96-well plate was placed in a CO_2-filled, sealed container, containing a high-transmission glass window (Edmund Optics). Wells were illuminated from the top with 50 mW of a 660 nm CW diode laser (Newport Corp.) with a spot size of 2 mm (one quadrant of a well in a 96-well plate) for 15 min. After illumination, cells were allowed to incubate for an additional 72 h at 37 °C. Cells were then immunostained for p65 and analyzed by flow cytometry and by immunofluorescence imaging.

***ON*-Switch Photonic Gene Circuit ($p65_{nuc}$ on).** HeLa cells were then washed once with Optimem media. A 0.5 μL concentrated pellet of siRNA-Au nanoantennas (4.0 AR) functionalized with IκB siRNA was resuspended in 100 μL of Optimem media, gently mixed, and added to each well of the 96-well plate. The cells were allowed to incubate for 4 h at 37 °C. After internalization of siRNA-Au nanoantennas for 4 h, the media was replaced with fresh supplemented DMEM culture media. The 96-well plate was placed in a CO_2-filled, sealed container, containing a high-transmission glass window (Edmund Optics). Wells were illuminated from the top with 50 mW of a 785 nm CW diode laser (Newport Corp.) with a spot size of 2 mm (one quadrant of a well in a 96-well plate) for 15 min. After illumination, cells were allowed to incubate for an additional 72 h at 37 °C. Cells were either immunostained for IκB and analyzed by flow cytometry or immunostained for p65 and analyzed by immunofluorescence imaging.

***PULSE*-Switch Photonic Gene Circuit (IP-10 on, RANTES off).** HeLa cells were then washed once with Optimem media. A 0.5 μL concentrated pellet of siRNA-Au nanoantennas (4.0 AR) functionalized with IκB siRNA was added to a 0.5 μL concentrated pellet of siRNA-Au nanoantennas (2.5 AR) functionalized with p65 siRNA and was resuspended in 200 μL of Optimem media, gently mixed, and added to each well of the 96-well plate. The cells were allowed to incubate for 4 h at 37 °C. After internalization of siRNA-Au nanoantennas for 4 h, the media was replaced with fresh supplemented DMEM culture media. The 96-well plate was placed in a CO_2-filled, sealed container, containing a high-transmission glass window (Edmund Optics). Wells were illuminated from the top with 50 mW of a 785 nm CW diode laser (Newport Corp.) with a spot size of 2 mm (one quadrant of a well in a 96-well plate) for 15 min. Two hours after initial illumination with 785 nm light, wells were illuminated from the top with 50 mW of a 660 nm CW diode laser (Newport Corp.) with a spot size of 2 mm (one quadrant of a well in a 96-well plate) for 15 min. After illumination, cells were allowed to incubate for an additional 72 h at 37 °C. The media was replaced with fresh supplemented DMEM culture media containing 3 μm monensin (Sigma) 48 h after illumination. The cells were allowed to incubate for an additional 24 h at 37 °C. Cells were then immunostained for IP-10 or RANTES and analyzed by flow cytometry.

Immunostaining for Flow Cytometry Analysis. Fluorescently labeled antibodies recognizing p65 and IκB were purchased from Santa Cruz Biotechnologies. Fluorescently labeled normal mouse isotype antibodies were also purchased from Santa Cruz Biotechnologies and were used as negative controls. The isotype control and fluorescently labeled antibodies recognizing IP-10 and RANTES were purchased from R&D Systems. Permeabilization buffer, for use with p65 and IκB antibodies, was prepared by adding 0.1% (w/v) saponin, 0.3% (w/v) Triton-X, and 0.1% (w/v) NaN_3 to Hank's balanced salt solution (Invitrogen). Permeabilization buffer, for use with IP-10 and RANTES antibodies, was prepared by adding 0.1% (w/v) saponin and 0.06% (w/v) NaN_3 to Hank's balanced salt solution (Invitrogen).

Cells were harvested, resuspended in 250 μL of 1× PBS, and fixed with 250 μL of 4% paraformaldehyde for 10 min. After 10 min, excess paraformaldehyde was removed by centrifuging and resuspending cells in 400 μL of permeabilization buffer (repeated twice). Cells were then counted to ensure all samples contained the same number of cells prior to immunostaining. For 50 000 cells, 10 μL of antibody or isotype antibody was added. Cells were gently mixed and incubated at room temperature for 45 min. After 45 min, excess antibodies were removed by centrifuging and resuspending cells in 400 μL of permeabilization buffer. To remove permeabilization buffer, cells were finally centrifuged and resuspended in 500 μL of 1× PBS. A LSRII flow cytometer (BD Biosciences) and FlowJo software (Tree Star, Ashland, OR, USA) were used to analyze samples.

Immunostaining of p65 for Immunofluorescence Imaging. Seventy-two hours after optical gene silencing of IκB or p65, cells (adhered to glass coverslips) were fixed in cold 50% methanol for 3 min on ice followed by cold 100% methanol for 15 min on ice. Cells were washed three times with and incubated in 1× PBS for 5 min on a rocker at ∼100 rpm speed. Cells were blocked with 5% normal mouse serum (Invitrogen) in 1× PBS for 30 min on a rocker at ∼100 rpm. Cells were washed two times with and incubated in 1× PBS for 5 min on a rocker at ∼100 rpm. Cells were then incubated in 300 nM DAPI (Invitrogen) in 1× PBS for 5 min in the dark on a rocker at ∼100 rpm. Cells were washed with and incubated in 1× PBS for 5 min on a rocker at ∼100 rpm. To 200 μL of 1× PBS was added 60 μL of AF488-labeled anti-p65 (Santa Cruz Biotechnologies). Cells were allowed to incubate for 2 h in the dark on a rocker at ∼100 rpm. Cells were washed three times with and incubated in 1× PBS for 5 min on a rocker at ∼100 rpm. The coverslip containing fixed, stained, adhered cells was finally placed face down on a microscope slide, sealed, and imaged using fluorescence microscopy.

Conflict of Interest: The authors declare no competing financial interest.

Acknowledgment. The authors acknowledge the National Institutes of Health (NIH) Nanomedicine Development Center for the Optical Control of Biological Function (PN2 EY018241) and the Center for Nanostructured Materials and Technology (CNMT) of the Korean government for financial support of the project. S.E.L. was supported by the Siebel Scholarship (Siebel Foundation) for the initial phase and the NIH Ruth L. Kirschstein National Research Service Award (F32 EB013972) for the final phase of the project. D.Y.S. was supported by the Division of Materials Science and Engineering in the Department of Energy, Office of Basic Energy Sciences, at Sandia National Laboratories, a multiprogram laboratory operated by Sandia Corp., a Lockheed Martin Co., for the U.S. Department of Energy (contract no. DE-AC04-94AL85000). M.J.B. was supported by the U.S. Department of Energy, Office of Biological and Environmental Research, and Low Dose Radiation Program (contract no. DE-AC02-05CH1123) and the Bay Area Physical Sciences−Oncology Center, University of California, Berkeley, CA 94720, USA (NCI U54CA143836). R.X. was supported by the American Heart Association (AHA 12SDG8600000). The authors thank Prof. Han Lim (UC Berkeley) for insightful discussions on modeling gene circuits. The authors also thank Ann Fischer and Michelle Yasukawa of the UC Berkeley Tissue Culture Facility for long-term maintenance of the HeLa cell line.

Supporting Information Available: This material is available free of charge *via* the Internet at http://pubs.acs.org.

REFERENCES AND NOTES

1. Lee, S. E.; Lee, L. P. Nanoplasmonic Gene Regulation. *Curr. Opin. Chem. Biol.* **2010**, *14*, 623–633.
2. Pastrana, E. Optogenetics: Controlling Cell Function with Light. *Nat. Methods* **2010**, *8*, 24–25.
3. Hamad-Schifferli, K.; Schwartz, J. J.; Santos, A. T.; Zhang, S.; Jacobson, J. M. Remote Electronic Control of DNA Hybridization through Inductive Coupling to an Attached Metal Nanocrystal Antenna. *Nature* **2002**, *415*, 152–155.
4. Lee, S. E.; Liu, G. L.; Kim, F.; Lee, L. P. Remote Optical Switch for Localized and Selective Control of Gene Interference. *Nano Lett.* **2009**, *9*, 562–570.
5. Lee, S. E.; Sasaki, D. Y.; Perroud, T. D.; Yoo, D.; Patel, K. D.; Lee, L. P. Biologically Functional Cationic Phospholipid-Gold Nanoplasmonic Carriers of RNA. *J. Am. Chem. Soc.* **2009**, *131*, 14066–14074.
6. Barhoumi, A.; Huschka, R.; Bardhana, R.; Knight, M. W.; Halas, N. J. Light-Induced Release of DNA from Plasmon-Resonant Nanoparticles: Towards Light-Controlled Gene Therapy. *Chem. Phys. Lett.* **2009**, *482*, 171–179.
7. Braun, G. B.; Pallaoro, A.; Wu, G.; Missirlis, D.; Zasadzinski, J. A.; Tirrell, M.; Reich, N. O. Laser-Activated Gene Silencing *via* Gold Nanoshell-siRNA Conjugates. *ACS Nano* **2009**, *3*, 2007–2015.
8. Chen, C.; Lin, Y.; Wang, C.; Tzeng, H.; Wu, C.; Chen, Y.; Chen, C.; Chen, L.; Wu, Y. DNA-Gold Nanorod Conjugates for Remote Control of Localized Gene Expression by Near Infrared Irradiation. *J. Am. Chem. Soc.* **2006**, *128*, 3709–3715.
9. Huschka, R.; Zuloaga, J.; Knight, M. W.; Brown, L. V.; Nordlander, P.; Halas, N. J. Light-Induced Release of DNA from Gold Nanoparticles: Nanoshells and Nanorods. *J. Am. Chem. Soc.* **2011**, *133*, 12247–12255.
10. Jones, M. R.; Millstone, J. E.; Giljohann, D. A.; Seferos, D. S.; Young, K. L.; Mirkin, C. A. Plasmonically Controlled Nucleic Acid Dehybridization with Gold Nanoprisms. *Chem. Phys. Chem.* **2009**, *10*, 1461–1465.
11. Kuo, T.; Hovhannisyan, V. A.; Chao, Y.; Chao, S.; Chiang, S.; Lin, S.; Dong, C.; Chen, C. Multiple Release Kinetics of Targeted Drug from Gold Nanorod Embedded Polyelectrolyte Conjugates Induced by Near-Infrared Laser Irradiation. *J. Am. Chem. Soc.* **2010**, *132*, 14163–14171.
12. Lu, W.; Zhang, G.; Zhang, R.; Flores, L. G.; Huang, Q.; Gelovani, J. G.; Li, C. Tumor Site-Specific Silencing of NF-kB p65 by Targeted Hollow Gold Nanosphere-Mediated Photothermal Transfection. *Cancer Res.* **2010**, *70*, 3177–3188.
13. Poon, L.; Zandberg, W.; Hsiao, D.; Erno, Z.; Sen, D.; Gates, B. D.; Branda, N. R. Photothermal Release of Single-stranded DNA from the Surface of Gold Nanoparticles through Controlled Denaturing and Au-S Bond Breaking. *ACS Nano* **2010**, *4*, 6395–6403.
14. Thibaudau, F. Ultrafast Photothermal Release of DNA from Gold Nanoparticles. *J. Phys. Chem. Lett.* **2012**, *3*, 902–907.
15. Wijaya, A.; Schaffer, S. B.; Pallares, I. G.; Hamad-Schifferli, K. Selective Release of Multiple DNA Oligonucleotides from Gold Nanorods. *ACS Nano* **2009**, *3*, 80–86.
16. Yamashita, S.; Fukushima, H.; Akiyama, Y.; Niidome, Y.; Mori, T.; Katayama, Y.; Niidome, T. Controlled-Release System of Single-Stranded DNA Triggered by the Photothermal Effect of Gold Nanorods and Its in Vivo Application. *Bioorg. Med. Chem.* **2011**, *19*, 2130–2135.
17. Hauck, T. S.; Jennings, T. L.; Yatsenko, T.; Kumaradas, J. C.; Chan, W. C. Enhancing the Toxicity of Cancer Chemotherapeutics with Gold Nanorod Hyperthermia. *Adv. Mater.* **2008**, *20*, 3832–3838.
18. Huang, X.; El-Sayed, I. H.; Qian, W.; El-Sayed, M. A. Cancer Cell Imaging and Photothermal Therapy in the Near-Infrared Region by Using Gold Nanorods. *J. Am. Chem. Soc.* **2006**, *128*, 2115–2120.
19. Khlebtsov, B.; Zharov, V.; Melnikov, A.; Tuchin, V.; Khlebtsov, N. Optical Amplification of Photothermal Therapy with Gold Nanoparticles and Nanoclusters. *Nanotechnology* **2006**, *17*, 5167–5179.
20. Lal, S.; Clare, S. E.; Halas, N. J. Nanoshell-Enabled Photothermal Cancer Therapy: Impending Clinical Impact. *Acc. Chem. Res.* **2008**, *41*, 1842–1851.
21. Link, S.; El-Sayed, M. Shape and Size Dependence of Radiative, Non-Radiative and Photothermal Properties of Gold Nanocrystals. *Int. Rev. Phys. Chem.* **2000**, *19*, 409–453.
22. Liu, G. L.; Kim, J.; Lu, Y.; Lee, L. P. Optofluidic Control of Photothermal Nanoparticles. *Nat. Mater.* **2006**, *5*, 27–32.
23. Svoboda, K. Biological Applications of Optical Forces. *Annu. Rev. Biophys. Biomol. Struct.* **1994**, *23*, 247–285.
24. Cubukcu, E.; Yu, N.; Smythe, E. J.; Diehl, L.; Crozier, K. B.; Capasso, F. Plasmonic Laser Antennas and Related Devices. *IEEE J. Sel. Top. Quantum Electron.* **2008**, *14*, 1448–1461.
25. Schuller, J. A.; Barnard, E. S.; Cai, W.; Jun, Y. C.; White, J. S.; Brongersma, M. L. Plasmonics for Extreme Light Concentration and Manipulation. *Nat. Mater.* **2010**, *9*, 193–204.
26. Skirtach, A. G.; Dejugnat, C.; Braun, D.; Susha, A. S.; Rogach, A. L.; Parak, W. J.; Mohwald, H.; Sukhorukov, G. B. The Role of Metal Nanoparticles in Remote Release of Encapsulated Materials. *Nano Lett.* **2005**, *5*, 1371–1377.
27. Sonnichsen, C.; Reinhard, B. M.; Liphardt, J.; Alivisatos, A. P. A Molecular Ruler Based on Plasmon Coupling of Single Gold and Silver Nanoparticles. *Nature Biotechnol.* **2005**, *23*, 741–745.
28. Liu, G. L.; Yin, Y.; Kunchakarra, S.; Mukherjee, B.; Gerion, D.; Jett, S. D.; Bear, D. G.; Gray, J. W.; Alivisatos, A. P.; Lee, L. P.; Chen, F. F. A Nanoplasmonic Molecular Ruler For Measuring Nuclease Activity and DNA Footprinting. *Nature Nanotechnol.* **2006**, *1*, 47–52.
29. Hoffman, A.; Levchenko, A.; Scott, M. L.; Baltimore, D. The IkB-NFkB Signaling Module: Temporal Control and Selective Gene Activation. *Science* **2002**, *298*, 1241–1245.
30. Bowen, G. P.; Borland, S. L.; Lam, M.; Libermann, T. A.; Wong, N. C. W.; Muruve, D. A. Adenovirus Vector-Induced Inflammation: Capsid Dependent Induction of the C-C Chemokine RANTES Requires NF-kB. *Hum. Gene Ther.* **2002**, *13*, 367–379.
31. Batchelor, E.; Loewer, A.; Lahav, G. The Ups and Downs of p53: Understanding Protein Dynamics in Single Cells. *Nat. Rev. Cancer* **2009**, *9*, 371–377.
32. Ekici, O.; Harrison, R. K.; Durr, N. J.; Eversole, D. S.; Lee, M.; Ben-Yaker, A. Thermal Analysis of Gold Nanorods Heated with Femtosecond Laser Pulses. *J. Phys. D: Appl. Phys.* **2008**, *41*, 185501.
33. Vieweger, M.; Goicocheo, N.; Koh, E. S.; Dragnea, B. Photothermal Imaging and Measurement of Protein Shell Stoichiometry of Single HIV-1 Gag Virus-like Nanoparticles. *ACS Nano* **2011**.
34. Braun, D.; Libchaber, A. Trapping of DNA by Thermophoretic Depletion and Convection. *Phys. Rev. Lett.* **2002**, *89*, 188103-1–4.
35. Alon, U. *An Introduction to Systems Biology*; CRC Press: Boca Raton, FL, 2007.
36. Rosi, N. L.; Giljohann, D. A.; Thaxton, C. S.; Lytton-Jean, A. K. R.; Han, M. S.; Mirkin, C. A. Oligonucleotide-Modified Gold Nanoparticles for Intracellular Gene Regulation. *Science* **2006**, *312*, 1027–1030.
37. Barlett, D.; Davis, M. Effect of siRNA Nuclease Stability on the in Vitro and in Vivo Kinetics of siRNA-Mediated Gene Silencing. *Biotechnol. Bioeng.* **2007**, *97*, 909–921.
38. Gou, L.; Murphy, C. J. Fine-Tuning the Shape of Gold Nanorods. *Chem. Mater.* **2005**, *17*, 3668–3672.
39. Nikoobakht, B.; El-Sayed, M. A. Preparation and Growth Mechanism of Gold Nanorods (NRs) Using Seed-Mediated Growth Method. *Chem. Mater.* **2003**, *15*, 1957–1962.
40. Huang, X. Gold Nanoparticles Used in Cancer Cell Diagnostics, Selective Photothermal Therapy and Catalysis of NADH Oxidation Reaction. Ph.D. thesis, Georgia Tech, 2006.
41. Sonnichsen, C. Plasmons in Metal Nanostructures. Ph.D. thesis, Ludwig-Maximilians-University of Munich, 2001.